Benchmarking of codes for electron cyclotron heating and electron cyclotron current drive under ITER conditions

R. Prater,[1] D. Farina,[2] Yu. Gribov,[3] R.W. Harvey,[4] A.K. Ram,[5] Y.-R. Lin-Liu,[6] E. Poli,[7] A.P. Smirnov,[4] F. Volpe,[8] E. Westerhof,[9] A. Zvonkov,[10] and ITPA Steady State Operation Topical Group

[1]General Atomics, P.O. Box 85608, San Diego, California 92186-5608, USA

[2]Associazione Euratom-ENEA-CNR sulla Fusione, IFP-CNR, Milano, Italy

[3]ITER International Team, Naka Joint Work Site, Ibaraki-ken, Japan

[4]CompX, Del Mar, California, USA

[5]Massachusetts Institute of Technology, Cambridge, Massachusetts, USA

[6]Department of Physics, National Central University and National Dong Hwa University, Taiwan

[7]Max Planck Institut für Plasmaphysik, EURATOM Association, Garching, Germany

[8]EURATOM/UKAEA Fusion Association, Culham Science Centre, Abingdon, UK

[9]FOM-Institute for Plasma Physics Rijnhuizen, Association EURATOM-FOM, Trilateral Euregio Cluster, The Netherlands (www.rijnh.nl)

[10]Nuclear Fusion Institute, RRC 'Kurchatov Institute', Moscow, Russia

e-mail: prater@fusion.gat.com

Abstract. Optimal design and use of electron cyclotron heating (ECH) requires that accurate and relatively quick computer codes be available for prediction of wave coupling, propagation, damping, and current drive at realistic levels of EC power. To this end, a number of codes have been developed in laboratories worldwide. A detailed comparison of these codes is desirable since they use a variety of methods for modeling

the behavior and effects of the waves. The approach used in this benchmarking study is to apply these codes to a small number of representative cases. Following minor remedial work on some codes, the agreement between codes for off-axis application is excellent. The largest systematic differences are found between codes with weakly relativistic and fully relativistic evaluation of the resonance condition, but even there the differences amount to less than 0.02 in normalized minor radius. For some other cases, for example for central current drive, the code results may differ significantly due to differences in the physics models used.

PACS Numbers: 52.35.Hr, 52.50.Sw, 52.55.Wq

1. Introduction

A system for Electron Cyclotron Heating (ECH) and Electron Cyclotron Current Drive (ECCD) is planned for ITER. This system may be used for plasma initiation and startup, electron heating, and current drive for the purposes of control of the equilibrium current profile and control of MHD instabilities like sawteeth and neoclassical tearing modes (NTMs). Theory and experiments have both shown that highly accurate placement of a narrow profile of ECCD can effectively suppress or reduce the size of NTMs. The ability to accurately predict the location and profile of ECH and ECCD is critical to an assessment of the power needed for these objectives in ITER. In this paper, several computational approaches to modeling ECH/ECCD effects under ITER conditions are compared for two cases, one at the scenario density and one at higher density, as a means of comparing the different physics models and implementations.

Section 2 of this paper describes the codes used in this study. Section 3 describes the conditions of the standard ITER case. In section 4 the results of the code comparison are presented, section 5 describes results for a test case with higher electron density where refraction is more significant. The results of this benchmarking study are discussed in section 6 and conclusions are presented in section 7.

2. The codes used

ECH codes are used to calculate the propagation of EC waves from the antenna to the plasma and within the plasma, the absorption of waves in the plasma, and current drive which may be generated by the waves [1]. The codes may be divided into groups according to their model of propagation, which may be described as ray tracing, Gaussian beam propagation, or quasi-optical propagation. The absorption of waves may be calculated in two basic ways. In the first, the absorption is found from an analytic model evaluated at points along the ray trajectory, and in the second the Fokker-Planck equation is solved in the quasi-linear approximation [2]. Similarly, the current drive may be calculated by an analytic solution to the adjoint equation [3], or in Fokker-Planck codes the current is simply found from the first moment of the distribution function. The codes which were used in this study are representative but not exhaustive of the codes in use. Their properties are summarized in table 1 and described below.

2.1. Ray tracing codes

In ray tracing codes the propagation is based on the model of geometric optics in nonuniform media given fully in Friedland and Bernstein [4]. In this model the ray trajectory and the ray wave number are advanced along the ray through derivatives of the dispersion relation. In the ray tracing model, the Gaussian beam is modeled as a number of rays arranged in space so that the spatially averaged power density along the ensemble approximates that of a propagating Gaussian beam, at least over some propagation range. The rays propagate independently and do not interact; therefore, such effects as diffraction and interference are not obtained with this formalism. The absorption along each ray is also calculated independently of other rays, so different rates of absorption may cause the radial profile of power in the beam to no longer resemble a Gaussian, which may be a real and important physical effect in some cases, particularly where the beam approaches the resonance at a steep angle. This distortion of the beam is calculated

in the approximation that partial absorption of part of the beam has no effect on the propagation of the other rays. Typically 30 to 100 rays are adequate to simulate a beam.

2.1.1. TORAY. The TORAY code [5] is an adaptation to tokamak geometry of earlier work done for mirror geometry. TORAY diverged into TORAY-GA, following work by Matsuda [6] and many others, and into TORAY-FOM following work by Westerhof [7]. These codes use the cold plasma dispersion relation for the ray tracing and various models may be chosen for the absorption. In this work the relativistic model by Mazzucato [8] is used for absorption in the TORAY-GA calculations and choice of a weakly relativistic model [7] derived by Westerhof or a fully relativistic model is used in TORAY-FOM. For ECCD, both codes may use the adjoint approach [9] specialized to ECCD by Cohen [3], with TORAY-FOM using the bounce-average option and TORAY-GA using the square magnetic well option. The Cohen approach has been reworked by Lin-Liu [10] to generalize the square magnetic well used in Cohen's approach to arbitrary geometry, and this is alternatively called by TORAY-GA. In a third version of the ECCD calculation, Lin-Liu has added the effect of the wave polarization calculated from an externally evaluated dispersion relation (in the present case, that from Ref. 8) rather than the approximation used in Refs. 3 and 10 that the wave is either right-hand circularly polarized or linearly polarized parallel to the magnetic field.

2.1.2. GENRAY. The highly modular GENRAY code [11] was developed to simplify the use of different dispersion relations for the ray tracing and absorption. Derivatives of the dispersion relation may be done either analytically, if available, or numerically. In this benchmarking study using the density characteristic of ITER Scenario 2, the ray tracing has been done using the fully relativistic dispersion relation [8]. For ECCD GENRAY uses the Cohen formulation [3].

GENRAY has also been coupled to two other dispersion relation models. In one, the dispersion relation is calculated by the R2D2 [12] code fully relativistically without

making the usual approximation that the dielectric tensor elements can be expanded as a truncated power series of $k_\perp \rho_e$. The second model for the dispersion relation is due to work by Westerhof [13] and Tokman [14], which described the breakdown of standard ray tracing when the part of the dispersion relation responsible for the absorption becomes too large, as may happen near a cyclotron resonance. This new physics was implemented in GENRAY by Smirnov and Harvey [15].

2.1.3. CQL3D. The CQL3D code [16] solves the Fokker-Planck equation in the quasi-linear approximation to obtain wave absorption and current drive. (For an excellent review of Fokker-Planck codes see Ref. 2.) The code accepts as input the ray trajectories calculated by other codes, presently TORAY-GA or GENRAY, and uses the local parameters along each ray as inputs to the Fokker-Plank solver, using the Stix formulation [17] of EC-induced quasi-linear diffusion in velocity space. The Fokker-Planck approach permits a more sophisticated model for the collision operator than the high velocity limit of the collision operator commonly used in the adjoint approach. The collision operator used in CQL3D conserves momentum in electron-electron collisions, and this may be a significant effect in calculating current drive. This code also has the capability to include the effects of radial transport on the driven current profile, but in this study this capability was not exercised.

2.1.4. BANDIT-3D. The BANDIT-3D code [18] is a Fokker-Planck code similar to CQL3D, but it contains its own ray-tracing package using the cold plasma dispersion relation. The Fokker-Planck treatment is relativistic.

2.2. Gaussian beam codes

Gaussian beam codes were developed to address the shortcoming of the ray tracing codes when interference or diffraction is important. When a beam is launched with strong focusing, for example, the geometric optics of ray tracing codes may have the rays all

crossing at a single point in space in an unphysical manner, while a Gaussian beam code would find a diffraction-limited waist of nonzero radius.

2.2.1. TORBEAM. The TORBEAM code [19] uses the ray tracing formalism with a cold plasma dispersion relation to determine the trajectory for the beam center, but instead of tracing additional independent rays to find the beam cross-section, it uses a paraxial expansion [20] of the complex eikonal to describe the cross-section of the beam in a way which naturally preserves diffraction and interference effects. Absorption of the beam is calculated using either a weakly or a fully relativistic model as if all the power were in the central ray and then the decrement in power is spread across the beam cross-section. If the beam divergence is significant, the spread in $n_{\parallel}$ in different parts of the beam can affect the absorption, or if the beam approaches the resonance at a small angle the side of the beam nearer the resonance would be preferentially absorbed. Calculating absorption using only the central values misses both of these effects, although only in special cases like highly oblique approach of the wave to the resonance are these effects significant. TORBEAM uses the Cohen formulation for current drive.

2.2.2. OGRAY. The OGRAY code [21] combines Gaussian beam propagation with a Fokker-Planck solver. The FP equation is solved on flux surfaces where an analytic model indicates that absorption takes place. The weakly relativistic linear collision operator includes the effects of trapped particles.

2.3. Quasi-optical code

The quasi-optical GRAY code [22] traces rays to simulate a Gaussian beam, but unlike the ray tracing codes an interaction between the rays is maintained to preserve interference and diffraction effects [23]. The cold plasma dispersion relation is used in the ray tracing. Absorption is calculated independently along each ray. This approach reduces the limitations described above when the beam is forced to fit a Gaussian

distribution even when the absorption and refraction are nonuniform across the beam. The ECCD is calculated in GRAY using the adjoint model described by Farina [22], which uses the square magnetic well of the Cohen model [3] but avoids the assumption that the wave is either linearly or right-hand circularly polarized.

2.4. Limitation of the codes

The WKB approximation upon which all these codes are based is that the properties of the dielectric do not vary across the EC beam. A potential problem arises when the beam illuminates the resonance obliquely, as in the ITER case described here, so that there is a significant variation in the imaginary part of the dielectric across the beam at fixed path length from the launcher. The extreme of this is the case of a beam propagating parallel to but near a resonance, so that the side of the beam nearer the resonance is more strongly absorbed, distorting the wavefront and inducing diffraction. In this situation only a full wave code is fully descriptive. Among the codes used in this study, the GRAY code, with its ensemble of interacting rays, best approximates the refraction and diffraction of a beam with weakly asymmetric absorption. Pure beam codes, which force a Gaussian absorption profile, address this situation less well. In between are the ray tracing codes with independent rays. This approach doesn't address diffraction, but it has a more flexible absorption model. In most cases of interest, including the ITER case described in this paper, any asymmetric absorption of the beam occurs near the resonance where the power is fully absorbed, so the higher order effects on propagation have only a small effect on the ray trajectories. It should also be noted that all these codes require use of an evaluation of $n_{\parallel}$ in order to calculate the absorption, since $n_{\parallel}$ is needed to define the resonance in velocity space. Determining $n_{\parallel}$ must invoke a ray-tracing-like model in which the wavefront is decomposed into pieces with the absorption calculated for each piece. These effects may affect the absorption location or

profile. In Sections 3 and 4 it will be shown that for this benchmark case these effects are not significant.

3. ECH/ECCD on ITER

The ITER ECH system used in this benchmarking study was designed for control of MHD modes which require current drive at the $q = 2$ and/or $q = 3/2$ surfaces. The geometry and kinetic profiles are shown in figure 1. The plasma parameters correspond to the "Scenario 2" $Q = 10$ conditions, with toroidal field $B_t = 5.3$ T, plasma current $I_p = 15$ MA, central electron density 1.02×10^{20} m^{-3}, and central electron temperature 24.8 keV. The EC power at 170 GHz is launched from a location at $R = 6.4848$ m, $Z = 4.110$ m near the top of the plasma with a toroidal component which drives co-current and with a vertical component which places the current near the rational $q = 3/2$ surface at $\rho = 0.66$. (Here, ρ designates the square root of the normalized toroidal flux.) The EC launch angles are characterized by the poloidal steering angle α, defined as the angle between the horizontal plane (constant Z) and the poloidal component of the beam, and the toroidal steering angle β, defined as the angle between the beam and the poloidal plane. Then α and β are related to the polar angle θ and the azimuthal angle ϕ, the conventional Euler angles used by some codes, through the relationships $\theta = \mathrm{acos}(\cos\beta \sin\alpha)$ and $\phi = \pi + \mathrm{asin}(\sin\beta / \sin\theta)$.

In this study the remote steering concept is modeled following an early engineering design [24]. (A more recent description of the ECH launcher may be found in reference 25.) The power from the waveguide reflects from a fixed focusing mirror 45 cm from the launch point at the end of the waveguide, and the focus places a minimum in the radius of the beam about 35 cm from the mirror. Figure 2 shows the beam radius as a function of distance along the wave path. The Gaussian beam codes described above can model the actual Gaussian beam, but the ray tracing codes which use geometric optics cannot. As an approximation, the divergence of the Gaussian beam can be fitted to a cone in the range of interest, which is 1 to 1.5 m from the final mirror for interaction with the $q = 3/2$ surface for a range of equilibria. This cone has a divergence of 1.08 deg at $\exp(-2)$ in

power with a starting point 0.5 m behind the final mirror (dashed line in figure 2). In this study, the ray tracing codes used this divergence but started the cone at the final mirror at $R = 6.4848$ m and $Z = 4.110$ m.

In this benchmarking study, the EC beam starting conditions are chosen to be relevant to the objective of driving current at the $q = 3/2$ surface at $\rho = 0.66$. In order to pick appropriate starting angles, the TORAY-GA code was used to survey the results of a scan over a range of the two launching angles. The normalized minor radius at the peak of the driven current and the value of the peak of the driven current are shown in figure 3. The values chosen for this study are $\alpha = -63.5$ deg and $\beta = 22.0$ deg, which maximize the peak current density on the rational surface.

4. Results for benchmark case

The codes described in table 1 were run for the benchmarking case, although not all optional models were used. The approach used in this study was as follows:

1. Verify that the codes are using the same starting angles (which may be defined in different ways in the different codes).

2. Verify that the equilibrium actually used is the same.

3. Verify that the profiles of electron temperature and density actually used are the same.

4. Compare the trajectories of the central ray or center of the beam.

5. Compare the rate of absorption along the central ray.

6. Compare the profiles of absorbed power and current drive.

After the codes were run, the data calculated along the central ray were assembled in tables as a function of ray arc length s at increments of about 1 cm. The data included the values of the ray coordinates R and Z, toroidal angle ϕ, the normalized minor radius ρ (square root of the normalized toroidal flux), the local electron density n_e and temperature T_e, the magnetic field B, the index of refraction, the parallel index of refraction $n_{||}$, the imaginary part of the perpendicular component of the wave number k_i, the normalized power remaining in the ray, and in some cases the effectiveness of the current drive dI_{EC}/ds. It should be noted that Fokker-Planck codes do not calculate k_i or dI_{EC}/ds since absorption is calculated using the quasi-linear diffusion operator averaged over a flux surface rather than along a ray.

Some of these objectives may seem trivial, but in fact it took a couple of iterations of the run/submit/compare cycle before items (1) to (3) were satisfied. The ray starting

angles were independently tested by determining the launching angles of the beam or central ray from the spatial coordinates of the first two points along the ray. For all cases, the poloidal and toroidal angles of the ray were equal to the target starting angles within the uncertainty set by the numerical precision of the reported coordinates. The use of the same equilibrium was verified by comparing the values of ρ and B for each (R,Z) point along the ray with that calculated independently from the equilibrium. Again, after a couple of iterations, this agreement was within the numerical uncertainties of the location of the points. And the use of the same profiles of electron temperature and density was verified by comparing $n_e[\rho(s)]$ and $T_e[\rho(s)]$ from the codes with the values expected from the profiles shown in figure 1, again with excellent agreement.

The ray trajectories are affected by refraction in general, but in the Scenario 2 case the density is low enough that refraction is very minor. At the plasma boundary the density jumps from 0 to 5.6×10^{19} m^{-3}, and codes either project a decreasing density outside the plasma or more commonly apply Snell's law at the boundary. For 170 GHz and quasi-normal propagation, the cutoff density is 3.5×10^{20} m^{-3}, so at a density so much lower than the cutoff density the change in the index of refraction as the plasma edge is crossed is very small. Figure 4(a-c) show the major radius $R(s)$, elevation $Z(s)$, and toroidal angle $\phi(s)$ of the ray as a function of arc length s for all the codes as differences from a straight line starting at the antenna with the target launch angles. All the codes lie close to each other, although the points of BANDIT-3D are slightly offset from the others by 1 cm.

The parallel index of refraction $n_{\parallel}$ and the magnetic field B are very important in the evaluation of the wave absorption since they determine the resonance condition. For $n_{\parallel}$ all codes have values very close to each other and close to that of a straight line as shown in Figure 4(d). Likewise, the magnetic field is very close for all codes and close to that along the trajectory of a straight line, as shown in figure 4(e).

The rates of absorption of the central ray as it approaches the resonance are slightly different for the codes depending primarily on whether the code uses a weakly relativistic or a fully relativistic calculation of the Doppler-shifted relativistic resonance. In the fully relativistic case the resonance condition may be written $\omega = h\Omega_e/\gamma + k_\| v_\|$, where ω is the applied frequency, h is the harmonic number, Ω_e is the electron cyclotron frequency for cold electrons, and γ is the relativistic factor $\left[1 - v^2/c^2\right]^{-1/2}$. In the weakly relativistic case, γ is expanded as its first two terms, $\gamma = 1 + \frac{1}{2}v^2/c^2$. Figure 5 shows the imaginary part of the wave number for the codes, and the division into the two groups can be clearly seen. Figure 5(a) shows that the difference in ρ is only about 0.015, which is small compared to the width of the heating profile. For some situations, these differences between the fully and the weakly relativistic codes can be important.

The heating profiles are very similar for all codes as shown in figure 6(a). In all cases, the power is fully absorbed, but the curves differ a little in width and height. In this study, no careful comparison of the starting conditions for beam width for the codes has been done. It is hard to define an approach to comparing the width of the beam codes with the ray tracing codes since beam width quantities were not collected (and may not be available for some codes). The difference between the fully relativistic codes and the weakly relativistic codes seen for the central ray in figure 5 is not so apparent in the net profiles of power density realized for a large number of rays combined or for a Gaussian beam.

A similar result is obtained for the current density [figure 6(b)]. The differences in the widths of the profiles result in moderate differences in the peak current densities, as shown in table 2, but the integrated currents are close. A good measure of the total current is obtained by the CQL3D code, which has an improved model for the collision operator (that is, an operator which conserves momentum in electron-electron collisions and does not use the high velocity approximation). The current drive from the most sophisticated analytic models, which include polarization effects and accurate magnetic

geometry, is slightly smaller, and the Cohen model is yet smaller. The current drive from the BANDIT-3D code is an outlier to such a degree that it was not plotted in figure 6b.

In figure 6b the current densities reported by the codes were plotted directly, except for that from CQL3D, which differs from the other codes in two respects. First, this code regenerates the equilibrium to be up-down symmetric, which modifies the area elements. Second, it reports the local toroidal current density at the outboard midplane $j_{\phi mid}$ rather than an averaged toroidal current density $\bar{j}_\phi$. We define $\bar{j}_\phi = \delta I_\phi / \delta A$ where δI_ϕ is the toroidal current between two flux surfaces and δA is the area between the surfaces in the poloidal cross-section. Then $\bar{j}_\phi = \int j_\phi d\ell dx / \int d\ell dx$ where j_ϕ is the local toroidal current density, ℓ is the coordinate along the poloidal projection of a flux surface, and dx is the distance separating the two flux surfaces in the poloidal cross-section. Since $j_{||}/B$ is a flux function and $j_{||}/B = j_\phi/B_\phi$, then $j_\phi = j_{\phi mid} B_\phi / B_{\phi mid}$, and substituting this and $\delta x = \delta\psi/2\pi R B_p$ into the integrals above, and recognizing that $B_\phi R = F(\psi)$ is a flux function, $\bar{j}_\phi = j_{\phi mid} R_{mid} \langle R^{-2}\rangle / \langle R^{-1}\rangle$. (Here, $\langle\cdots\rangle$ denotes the flux surface average $\langle a \rangle = \oint a \frac{d\ell}{B} / \oint \frac{d\ell}{B}$.) This quantity is plotted for CQL3D in figure 6b. The TORBEAM code reports the flux-surface-averaged parallel current density $\bar{j}_{||}$ rather than $\bar{j}_\phi$, and this is plotted in figure 6b.

As an independent check on the integration in each code, the current profiles shown in figure 6b were integrated using the simple procedure $I_{ECCD} = \sum_i \bar{j}_{\phi i} \delta A_i$, where the cross-sectional area elements are

$$dA_i = \frac{1}{2\pi} \frac{dV}{d\rho}(\rho_i)\left\langle\frac{1}{R}\right\rangle\frac{\rho_{i+1} - \rho_{i-1}}{2} \quad .$$

Here, V is the volume enclosed by the flux surface as a function of ρ. For TORBEAM, $\bar{j}_\phi$ may be obtained from $\bar{j}_{||}$ by the expression

15

$$\bar{j}_\phi = \left[\frac{F(\psi)\langle R^{-2}\rangle}{\langle B\rangle\langle R^{-1}\rangle}\right]\bar{j}_\parallel \quad ,$$

where $F(\psi) = B_\phi R$ is a flux surface function. Using this process, the independent integrations are shown in table 2. These agree to within a few percent with the integrals done by the codes.

An interesting view of the detailed wave-particle interaction may be found from the Fokker-Planck solutions. The FP code CQL3D calculates the particle flux in velocity space which may illuminate the physics of ECCD under ITER conditions. Figure 7 shows the velocity space at the location of peak absorption of the central ray of the TORAY-GA calculation of the ray trajectory and absorption. The calculation is fully relativistic, but the results have been scaled from normalized momenta which are used by the code for relativistic effects to normalized velocities to correspond to the usual physics intuition for the wave-particle interaction. The yellow circular arcs represent contours of integral values of v/v_{th}, where v_{th} is the thermal velocity of the electrons, and the green lines divide the trapped electrons (large $v_\perp/v_\parallel$) from the passing electrons for the local value of the magnetic well depth. CQL3D evaluates the quasilinear diffusion operator over radial zones in order to calculate the effects on the distribution function. The fully relativistic resonance condition $\omega = \Omega_e/\gamma - k_\parallel v_\parallel$, is evaluated where the central ray crosses the two boundaries of the zone and shown as the two red curves in a figure 7.

The electron flux in velocity space due to the effect of the rf is shown as the magenta arrows in figure 7a. As expected, the flux generated by the EC waves is in the perpendicular direction. (The flux lying outside the region demarked by the resonance curves is due to the distribution of $k_\parallel$ for the array of 98 rays which cross the zone.) This flux is the reaction of the distribution function to the EC waves, the force term in the Fokker-Planck equation. By itself, this EC-induced flux is very ineffective in driving current because the flux in velocity space is nearly parallel to the contours of constant

velocity, while the current drive effect depends on increasing the velocity of the group of affected electrons in order to reduce their collisionality [26]. However, the equilibrium distribution function is determined by a balance between this force term and the relaxing effects of collisions. The net flux which creates this balance is shown in figure 7b. The effect of the EC waves is to set up a convective cell in which electrons flow away from the trapping region by pitch angle scattering along the constant energy contour $v/v_{th} = 2.2$ to the resonance region. In the region of the resonance, the net flux is parallel, the most effective direction for current drive. In order to have zero divergence, the flux then is directed back toward the trapping region by pitch angle scattering along $v/v_{th} = 3.3$. The flux pattern for lower hybrid current drive, for which the wave-particle interaction is mainly parallel rather than perpendicular as for EC waves, must look very similar to this, except that the distance in $v_{\parallel}/v_{th}$ may be larger between the flows toward and away from the resonance region.

5. High density benchmark case

It may be seen from figure 4 that the refraction is quite small for the ITER benchmark case. That is, the central ray trajectory varies very little from that of a straight line. Consequently, the propagation model was not well tested. In order to test refraction the electron density of the ITER Scenario 2 benchmark case was increased by a factor near 3 so that refraction would be stronger. In order to avoid problems with the benchmark profile which is nondifferentiable where the flat part of the profile ends, a smoothed density profile shown in figure 8 was substituted. (This smoothed profile was derived by dividing the pressure profile of the equilibrium by $T_e + T_i$ and multiplying by 3.)

Two dispersion relations were used in the high density benchmark that were not used for the standard density case: the R2D2 code [12] called from GENRAY, which is fully relativistic and which does not expand the dielectric tensor, and the Westerhof-Tokman dispersion relation [13,14], which addresses issues which arise when the absorption becomes sufficiently strong. The R2D2 code would not be expected to produce results greatly different than a fully relativistic code that does use an expansion in this benchmark case, since the product $k_\perp \rho_e \approx v_{th}/c$ is small, about 0.1. Since this is the argument for expansion of the Bessel functions, a small number of terms in the expansions should be adequate. (Recall that the cyclotron resonance is a wave-particle resonance and not a dielectric resonance, so effects on $k_\perp$ are weak.) Likewise for the Westerhof-Tokman correction, at the peak of absorption the ratio of the imaginary part of the wave number to the real part is only 10^{-2}. So strong modification of the dispersion relation would not be expected. Thirty rays were used in the calculations using these dispersion relations.

The ray trajectories are shown in figure 9, again as differences from a straight line. The ray ends about 6 cm away from the straight line, with most of the difference being in the direction of the major radius. Interestingly, the ray tracings using the R2D2 and the

Westerhof-Tokman codes showed moderately strong deviations from the ray tracing of the other codes but were rather similar to each other. The trajectories of the other codes are very close to each other except for the BANDIT-3D ray which showed the same deviation from the other codes as at lower density.

The imaginary part of the wave number for the higher density case is shown in figure 10. The division between weakly relativistic codes and fully relativistic codes is not as pronounced in this plot as it was in the standard density case. The effect is in the same direction, as seen for example in the two models in the GRAY code, but the difference is comparable to the code-to-code differences.

The current density and power density profiles show a little more deviation than at lower density, as shown in figure 11, due to the stronger refraction. The deviation in the normalized minor radius is still only about 0.02, as shown in table 3. The variation in the peaks between the different codes is caused mostly by the same issues about beam width as in the lower density case; nevertheless, the integrated currents shown in table 3 indicate good agreement.

6. Discussion

All of the codes produce calculations of the location of the absorption which are in acceptable agreement; that is, the differences between the peaks of the current density and power density profiles are much smaller than the width of the profiles, both for the benchmark case and the higher density case. As mentioned before, the widths of the profiles may vary because of different models of beam dispersion, and this was not independently compared. All of the codes calculate full absorption of the incident power.

This group of codes provides an interesting mix and match of models. We have codes like GENRAY (Fully rel., Cohen) and TORAY-GA (Fully rel., Cohen), which use identical models (same Fortran coding) both for absorption and current drive, but use a different ray-tracing model. These codes produce integrated currents which differ by 4% in the standard density case and 6% in the high density case. Using the independent integration of the current densities, the results are closer, 3% and 4%, respectively.

Another comparison can be made between codes with similar physics models but completely different coding. One good example here is the comparison of GRAY (Fully rel., Farina) with TORAY-GA (Fully rel., Lin-Liu, pol.). For both the standard density case and the high density case the codes differ by less than 2%, but using the independent integration the differences are closer to 1%.

The difference between fully relativistic and weakly relativistic models can be seen by comparing TORAY-FOM (fully relativistic, Cohen) with TORAY-FOM (weakly relativistic, Cohen). Here the fully relativistic calculation of ECCD is 5.5% larger than for weakly relativistic, with similar result using the independent integration. Similarly, the fully relativistic version of GRAY shows the same 5.5% increase over the weakly relativistic version, again with a similar result for the independent integration. The two weakly relativistic code versions which use Cohen, namely TORBEAM (weakly rel.) and TORAY-FOM (Weakly rel., Cohen), get results which differ by about 3%. As pointed

out by Poli [27], the difference in the magnetic field where the absorption takes place differs only very slightly between the weakly and fully relativistic resonances, but the effect on the driven current can be much larger due to the sensitivity of the current drive to shifts in velocity space.

The Fokker-Planck codes differ more widely in the standard density case. BANDIT-3D calculates 10900 A/MW, while CQL3D gets 8817 and OGRAY 8114. None of the FP codes shows significant quasilinear effects. The threshold for quasilinear effects was found by Harvey [28] to be when $2q_e / n_{19}^2 > 1$, where q_e is the power density in MW/m^3 and n_{19} is the density in units of $10^{19} m^{-3}$. For this standard density case, this criterion is only 4×10^{-4} for the benchmark calculation at a power level of 1 MW; even at 20 MW this criterion is well satisfied. In the higher density case the FP calculations are closer, differing by 6.6% between CQL3D and OGRAY. In general, the FP models have the advantage of using more accurate collision operators, while the analytic codes use collision models which use the high energy limit of the collision operator to facilitate the solution.

Comparing the best models available—that is, the fully relativistic absorption and the Farina or Lin-Liu current drive models, and the Fokker-Planck models excepting BANDIT-3D—the results are within ±5% for both the standard density and high-density cases. This level of uncertainty may be irreducible due to the differences in the physics models, which have different degrees of applicability and approximation. Some codes use a recalculated equilibrium, which may affect the areas between flux surfaces resulting in the differences between the internal and external integrations of current, depending on how the spline fittings are done. Another source of difference is that many codes use poloidal flux as their radial coordinate, and in rescaling to toroidal flux some level of uncertainty is introduced.

It would be incorrect to conclude from this work that all these different models should yield the same result if they were all implemented correctly. The different models

represent different physics and the choice of model must be made judiciously. We have seen above that the codes yield similar results for the benchmarking case or its high density variant. A counter example may be useful to illustrate how the models may differ under other conditions.

One other possible use of ECCD is central current drive, which may illuminate some differences between codes. In this exercise we consider application of EC waves from a midplane equatorial launch at R=9.628 m and Z=0.611 m. The ray bundle is launched in the horizontal plane, with a toroidal angle 12.3 deg from radial. In order to move the EC interaction to a small minor radius, we increase the toroidal field from 5.3 T to 5.63 T (this is a gedanken experiment), but the kinetic profiles are the same as the standard benchmark case.

The ECCD profiles resulting from running CQL3D and the three TORAY-GA variants show strong differences, as shown in figure 12. For TORAY-GA, the current drive models (Lin-Liu with polarization effects, Lin-Liu, and Cohen) produce net driven currents of 11.62, 10.34, and 10.05 kA/MW. But CQL3D, run at a power level of 1 kW to avoid the possibility of quasilinear effects in the calculation, finds 24.0 kA/MW. This factor 3 difference may be attributed to the more accurate collision model in CQL3D. The standard collision operator in CQL3D preserves momentum in collisions between electrons. For the benchmark case, the interaction is at $\rho = 0.66$ so many of the electrons are trapped in the magnetic well. Conserving momentum in collisions with trapped electrons is not effective in preserving the toroidal current. But for the central case, few electrons are trapped at small minor radius, so collision with these bulk-transiting electrons does not diminish the current drive, and the current drive efficiency is higher. CQL3D has the option of turning off the momentum conservation, and doing so reduces the current to 15.7 kA/MW. The remainder of the difference between that and the TORAY-GA level is believed due to the high velocity limit of the collision operator which the TORAY-GA code uses.

A final point which should be noted is that improvement of the codes is a valuable product of a benchmarking study like this one. A great many advances in the models available in the codes, improvements in the numerics, and elimination of errors have made the codes more accurate and complete.

7. Conclusions

The codes use a variety of models of wave propagation, absorption, and current drive, but the resulting profiles of heating and driven current are quite close for the ITER benchmarking case. The total driven currents have a range of 10%, with the Fokker-Planck models (and particularly CQL3D) larger than the analytic models, presumably due to a more physical collision model. The range of the peak driven current density is larger due to differences in the current drive profiles, with CQL3D having the narrowest profile as well as the largest driven current and hence the largest peak current density. The locations are quite close for all codes. A counter-example of agreement was provided for a case of central current drive, illustrating the need to be careful in choosing a code for any specific purpose. Quasi-linear effects are not significant under ITER conditions. Since some of the codes have been well validated against experiment under conditions not too far from the ITER conditions [29,30] it seems that the fully relativistic codes are well qualified to predict the EC performance in ITER. The Gaussian beam codes are better suited in cases where the focus of the EC beam lies well inside the plasma.

References

[1]   Prater R. 2003 Phys. Plasmas **5** 2349.

[2]   Westerhof E. 1995 Conf. Proc., 9th Joint Workshop on Electron Cyclotron Emission and Electron Cyclotron Heating, World Scientific, Singapore, p. 3.

[3]   Cohen R.H. 1987 Phys. Fluids **30** 2442.

[4]   Friedland L. and Bernstein I.B. 1980 Phys. Rev. A **22** 1680.

[5]   Kritz A.H., Hsuan H., Goldfinger R.C. and Batchelor D.C. 1982 Conf. Proc., 3rd Int. Symp. on Heating in Toroidal Plasmas ECE, Brussels, Vol. **2** 707.

[6]   Matsuda K. 1989 IEEE Trans. Plasma Science **17** 6.

[7]   Westerhof E. "Implementation of TORAY at JET," National Technical Information Service document no PB91-114819INZ (Rijnhuizen Report 89-183, 1989). Copies may be ordered from the National Technical Information Service, Springfield, Virginia 22161, USA.

[8]   Mazzucato E., Fidone I. and Granata G. 1987 Phys. Fluids **30** 3745.

[9]   Antonsen T.M. and Hui B. 1984 IEEE Trans. Plasma Sci. **PS-12** 118.

[10] Lin-Liu Y.R, Chan V.S. and Prater R. 2003 Phys. Plasmas **10** 4064.

[11] Harvey R.W. 1994 Bull. Am. Phys. Soc. **39** 1626.

[12] Ram A.K., Decker J. and Peysson Y. 2005 J. Plasma Physics **71** 675.

[13] Westerhof E. 1997 Plasma Phys. Control. Fusion **39** 1015.

[14] Tokman M.D., Westerhof E. and Gavrilova M.A. 2000 Plasma Phys. Control. Fusion **42** 91.

[15] Smirnov A.P., Harvey R.W., Westerhof E., Tokman M.D. and Balakina M.A. 2005 Proc. 13th, Joint Workshop on Electron Cyclotron Emission and Electron Cyclotron Heating, Nizhny Novgorod, Russia (2005 Institute of Applied Physics, Russian Academy of Sciences) p. 73.

[16] Harvey R.W. and McCoy M.G. IAEA Conf. Proc., Technical Committee Meeting on Advances in Simulation and Modeling of Thermonuclear Plasmas, June 15-18, 1998, Montreal, Canada, International Atomic Energy Agency, Vienna, Austria, 1993, p. 305.

[17] Stix T.H. Theory of Plasma Waves, 2nd ed. (Wiley, New York, 1992).

[18] O'Brien M.R., Cox M., Warick C.D. and Zaitsev F.S. IAEA Proc., Technical Committee Meeting on Advances in Simulation and Modeling of Thermonuclear Plasmas, June 15-18, 1998, Montreal, Canada, International Atomic Energy Agency, Vienna, Austria, 1992, p. 527.

[19] Poli E., Pereverzev G.V. and Peeters A.G. 1999 Phys. Plasmas **6** 5.

[20] Pereverzev G.V. 1998 Phys. Plasmas **5** 3529.

[21] Zvonkov A.V., Kuyanov A.Y., Skovoroda A.A. and Timofeev A.V. 1998 Plasma Phys. Reports **24** 389.

[22] Farina D. "GRAY: a quasi-optical ray tracing code for electron cyclotron absorption and current drive in tokamaks," IFP-CNR Internal Report FP 05/1 (2005), http://www.ifp.cnr.it/publications/2005/FP05-01.pdf.

[23] Mazzucato E. 1989 Phys. Fluids B **1** 1855.

[24] Graswinckel M., IAEA TM on ECRH Physics and Technology for ITER, 14-16 July 2003, Kloster-Seeon, Germany (IPP Garching, 2003).

[25] Ramoni, G. *et al.*, 2007 Fusion Sci. and Tech. **52** 193.

[26] Fisch N.J. and Boozer A.H. 1980 Phys. Rev. Lett. **45** 720.

[27] Poli E., Farina D., Henderson M.A, Prater R., Ramponi G., Saibene G. and Zohm H. "Performance studies for the ITER ECRH launcher," Proceedings of the 14th Joint Workshop on Electron Cyclotron Emission and Electron Cyclotron Resonance Heating EC-14, Santorini, Greece, May 9-12 2006 [Heliotopos Conferences Ltd, Athens, 2006], p. 301.

[28] Harvey R.W., McCoy M.G. and Kerbel G.D. 1989 Phys. Rev. Lett. **62** 426.

[29] Petty C.C., Prater R., Lohr J., Luce T.C., Fox W.R., Harvey R.W., Kinsey J.E., Lao L.L. and Makowski M.A. 2002 Nucl. Fusion **42** 1366.

[30] Suzuki T. *et al*. 2004 Nucl. Fusion **44** 699.

Table 1. ECH codes used in this benchmarking study.

Code	Propagation Model	Propagation Dispersion Relation	Resonance	Absorption	ECCD Model
BANDIT-3D	Rays	Cold	Relativistic	Fokker-Planck	Fokker-Planck
CQL3D	Rays	Cold	Relativistic	Fokker-Planck	Fokker-Planck
GENRAY	Rays	Relativistic	Relativistic	Mazzucato	Cohen
		Relativistic (R2D2)	Relativistic	R2D2	Cohen
		Relativistic (Westerhof-Tokman)	Relativistic	Relativistic	Cohen
GRAY	Quasi-optical	Cold	Relativistic	Analytic	Farina
			Weakly relativistic	Analytic	Farina
OGRAY	Gaussian	Cold	Relativistic	Fokker-Planck	Fokker-Planck
TORAY-FOM	Rays	Cold	Weakly relativistic	Westerhof	Cohen
		Cold	Relativistic	Westerhof	Cohen
TORAY-GA	Rays	Cold	Relativistic	Mazzucato	Cohen
				Mazzucato	Lin-Liu
				Mazzucato	Lin-Liu pol
TORBEAM	Gaussian	Cold	Weakly relativistic	Westerhof	Cohen
			Relativistic		Cohen

Table 2. Integrated currents from the codes. The first column lists the codes and the model used. The second column is the integrated current reported by the code. The third column is an independent integration of the current density profiles shown in figure 6. Also listed are the peak values of the ECCD current density, the ρ at which it peaks, and the full width $\delta\rho$ at 1/e.

Code	A/MW code	A/MW calc	j_{ECCD} $(A/cm^2/MW)$	ρ	$\delta\rho$
BANDIT-3D (FP)	10900	-	-	-	-
CQL3D (FP)	8817	8921	0.760	0.646	0.048
GRAY (Fully rel., Farina)	8586	8603	0.645	0.646	0.054
GRAY (Weakly rel., Farina)	8127	8147	0.631	0.639	0.053
GENRAY (Fully rel., Cohen)	7819	7808	0.557	0.641	0.057
OGRAY (FP)	8114	8306	0.631	0.639	0.053
TORAY-FOM (Fully rel., Cohen)	8410	8602	0.577	0.643	0.060
TORAY-FOM (Weakly rel., Cohen)	7970	8117	0.570	0.636	0.058
TORAY-GA (Fully rel., Lin-Liu, pol.)	8413	8488	0.681	0.641	0.051
TORAY-GA (Fully rel., Lin-Liu)	7999	8072	0.647	0.642	0.051
TORAY-GA (Fully rel., Cohen)	7461	7528	0.604	0.642	0.051
TORBEAM (Weakly rel., Cohen)	8268	8282	0.610	0.638	0.055
TORBEAM (Fully rel., Cohen)	8726	8668	0.639	0.644	0.054

Table 3. Integrated currents for the high-density case. The third column is the current calculated independently from the current density profiles in figure 11. The other columns have the same meaning as in Table 2.

Code	A/MW code	A/MW calc	j_{ECCD} $A/cm^2/MW$	ρ	$\delta\rho$
CQL3D (FP)	3832	3895	0.367	0.695	0.040
GRAY (Fully rel., Farina)	3710	3726	0.300	0.700	0.047
GRAY (Weakly rel., Farina)	3440	3512	0.286	0.694	0.046
GENRAY (Fully rel., Cohen)	3458	3471	0.296	0.693	0.045
GENRAY (R2D2, Cohen)	3545	3558	0.312	0.693	0.043
GENRAY (West.-Tokman, Cohen)	3511	3522	0.285	0.690	0.047
OGRAY (FP)	3514	3545	0.299	0.713	0.043
TORAY-GA (Fully rel., Lin-Liu, pol.)	3666	3751	0.289	0.693	0.049
TORAY-GA (Fully rel., Lin-Liu)	3505	3587	0.276	0.693	0.049
TORAY-GA (Fully rel., Cohen)	3260	3336	0.257	0.693	0.049
TORBEAM (Fully rel., Cohen)	3783	3693	0.267	0.697	0.051
TORBEAM (Weakly rel., Cohen)	3493	3338	0.244	0.691	0.051

LIST OF FIGURE CAPTIONS

Figure 1. (a) Cross-section of the ITER Scenario 2 plasma equilibrium used in this study. The solid flux surfaces are the rational surfaces $q = 2$ and $q = 3/2$. The ECH launcher is near the top of the plasma. Some typical ECH rays are shown for driving co-current at the $q = 3/2$ surface. The vertical line marked "1" is the fundamental resonance. The electron temperature profile (b) and plasma density profile (c) were provided by the ITER team.

Figure 2. Radius of the EC beam at $\exp(-2)$ in power as a function of distance along the wave arc length, reprinted from Ref. 24. The solid curve is for the design which includes a focusing mirror. The shaded region has been added to the original figure to show the approximate range to the interaction locations of interest. The dashed curve, which was also added to the figure, is an approximate fit to the divergence of the beam in the region of interest.

Figure 3. Ray tracing results from TORAY-GA code using 48 rays, for the geometry shown in figure 1, as a function of the poloidal steering angle α and toroidal steering angle β. Shown are the normalized minor radius ρ of the peak of the driven current (dashed contours) and the peak driven current in A/cm^2/MW (solid contours). The diamond symbol represents the chosen angles for this study, which correspond to the peak in driven current at the $q = 3/2$ surface located at $\rho = 0.66$.

Figure 4. Quantities (a) major radius R, (b) elevation Z, (c) and toroidal angle ϕ, plotted as the difference between the central ray and the values for a straight line (subscript SL) with the target values of the launching angles and location, for the codes of Table I. (d) Difference between $n_{\parallel}$ and the projection of a unit vector along the straight line on the magnetic field, and (e) the difference between B and an evaluation of the magnetic field along the straight line. All quantities are plotted as a function of arc length from the

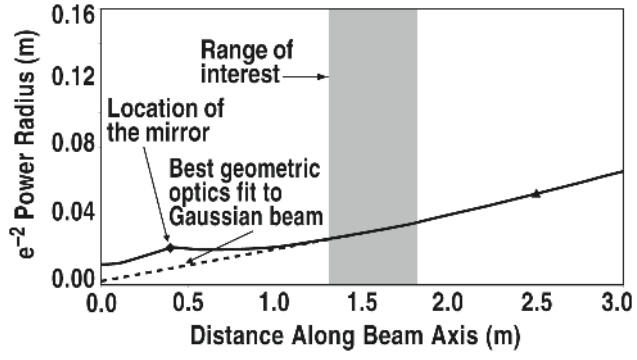nominal antenna location at $R = 6.4848$ m and $Z = 4.11$ m. The plasma edge is near 0.5 m arc length.

Figure 5. Imaginary part of the wave number as a function of (a) normalized minor radius and (b) arc length.

Figure 6. (a) Profile of electron power deposition for the codes, and (b) electron cyclotron current density profile.

Figure 7. Fluxes in velocity space calculated by CQL3D for the zone of largest wave-particle interaction. The yellow circular arcs are contours of integral values of v/v_{th}, the green lines are the trapped/passing boundary, and the red ellipses are the relativistic resonance for the central ray where it crosses the zone boundaries. The magenta arrows represent the direction and magnitude of the flux of electrons in velocity space, and the white shading represents the magnitude of the flux. a) Flux due to the EC source, and b) total flux including the effect of collisions.

Figure 8. Density profile used in the high density benchmarking.

Figure 9. Same as figure 4 but for the higher density profile.

Figure 10. The imaginary part of the wave number as a function of (a) normalized minor radius and (b) of arc length for the higher density case.

Figure 11. (a) Electron power density profile for the codes, and (b) electron cyclotron current density profile for the higher density case.
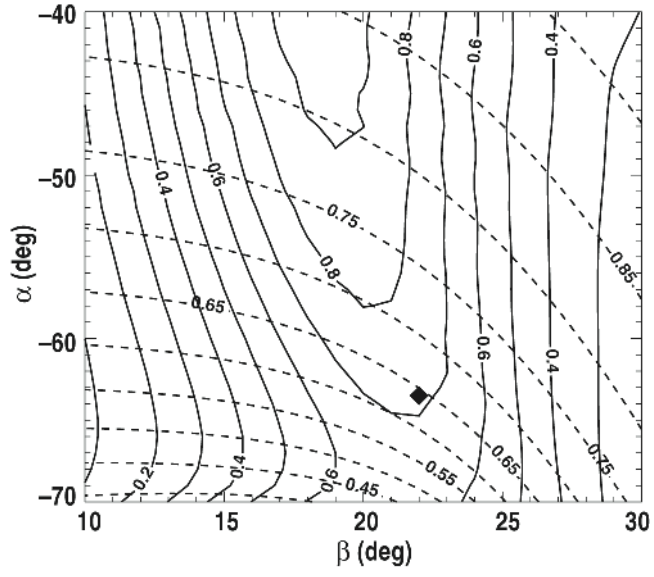
Figure 12. Current density profile calculated by CQL3D using the standard collision operator (solid black line) or the non-momentum-conserving operator (dashed line). Also shown are the TORAY-GA models by Cohen (red), Lin-Liu (blue), and Lin-Liu including polarization effects (green).
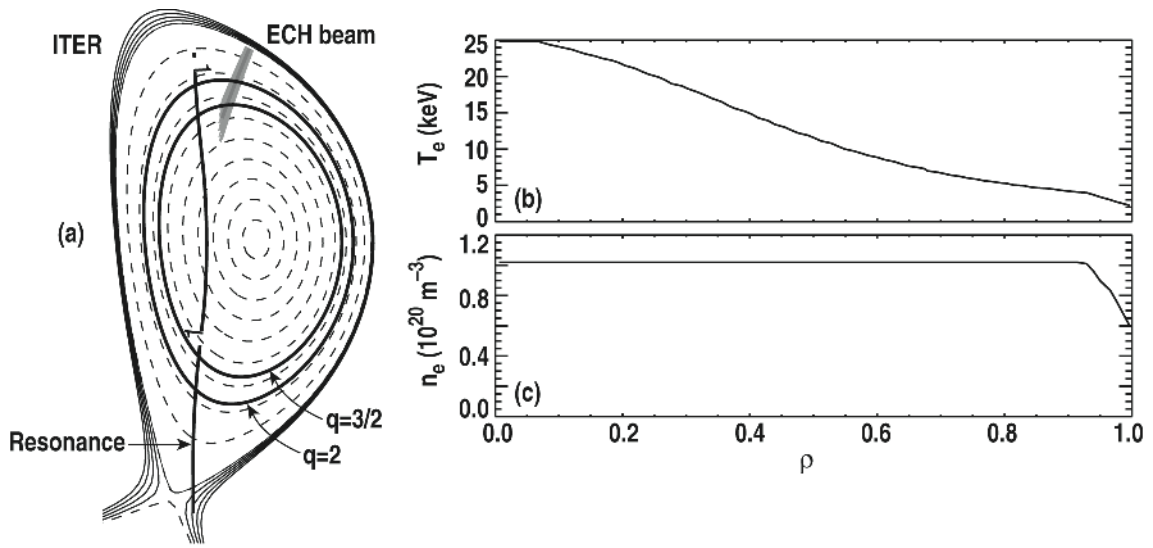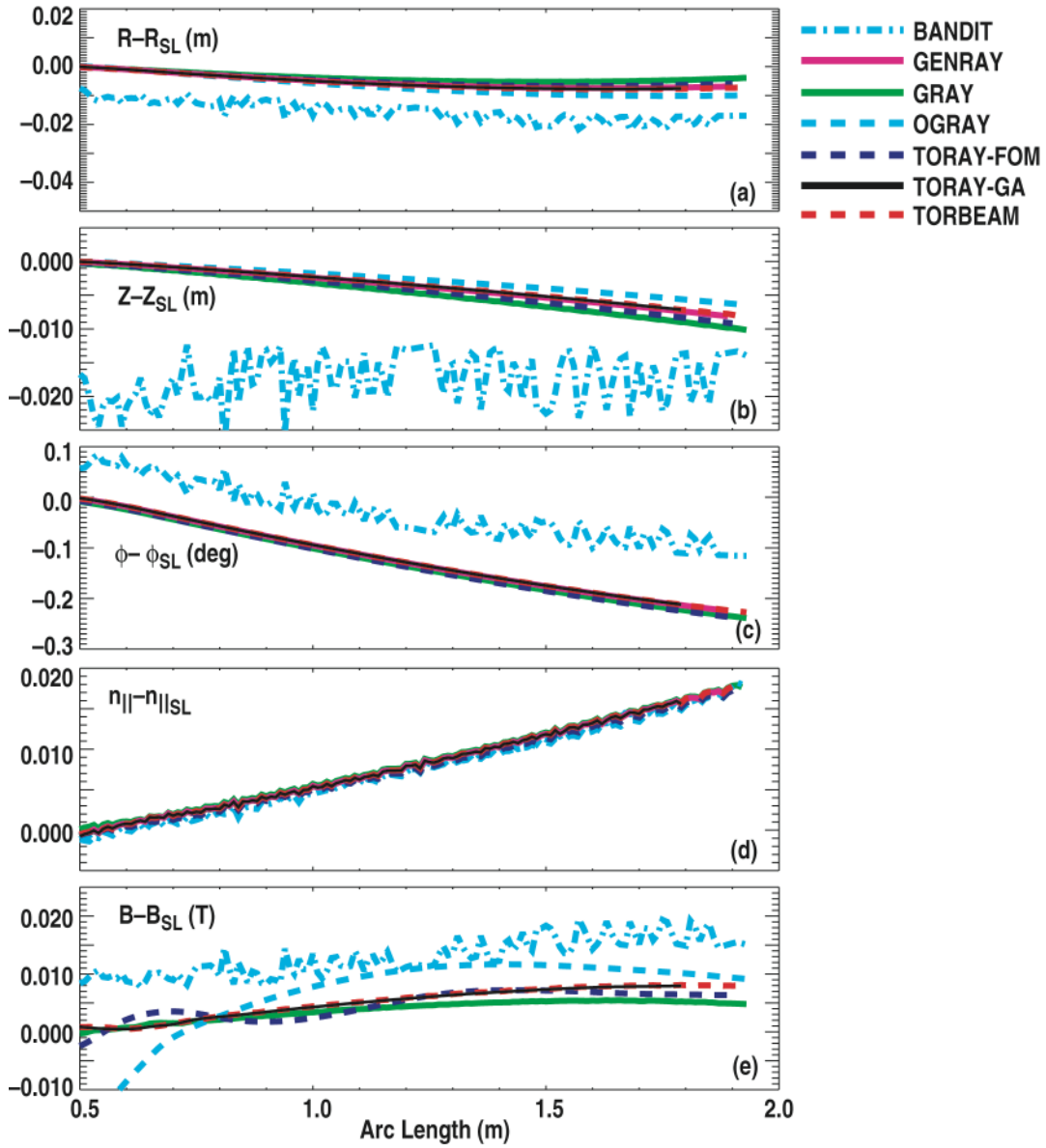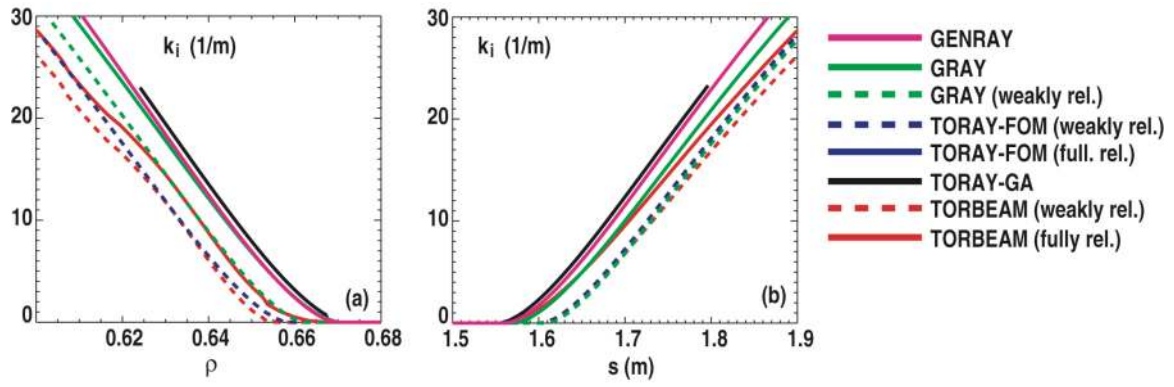
NF_256426_PAP_5616, R. Prater, Figure 1

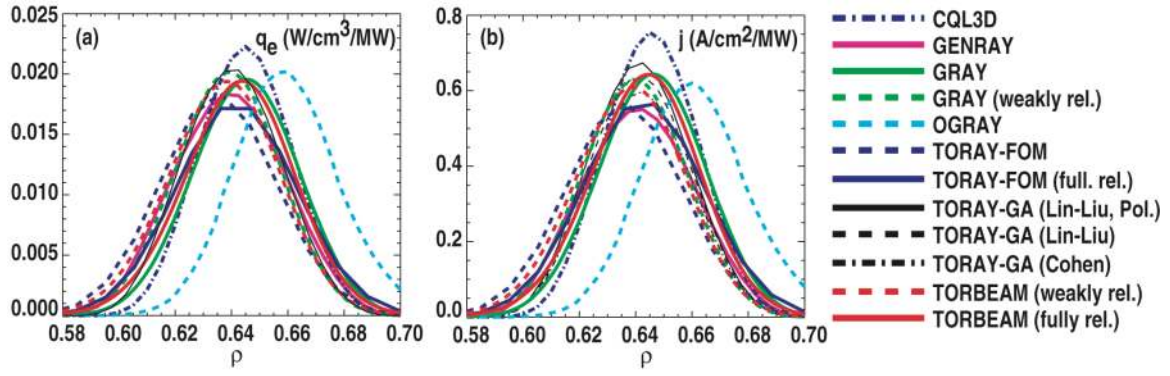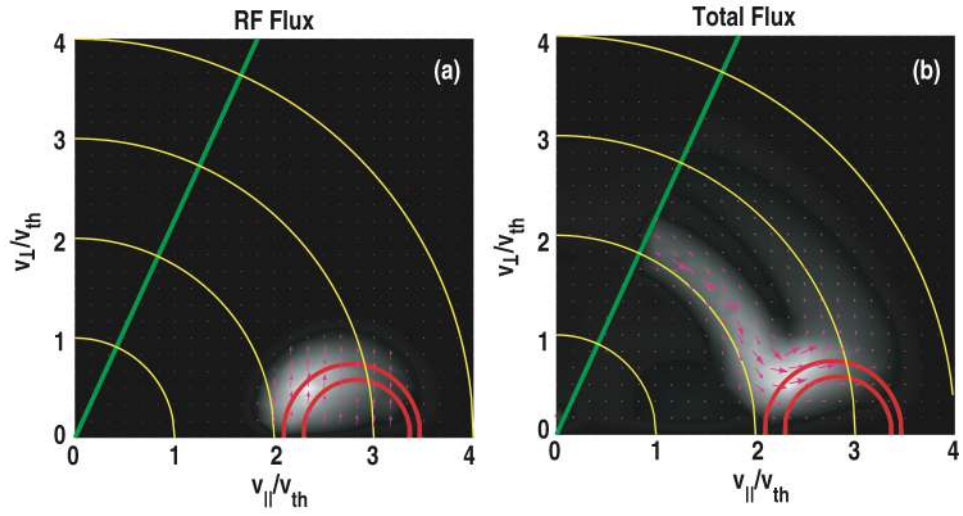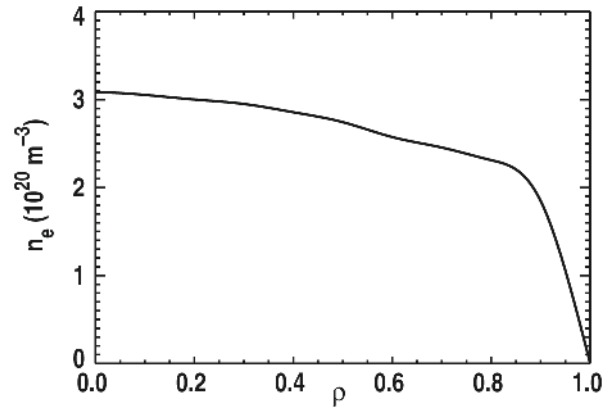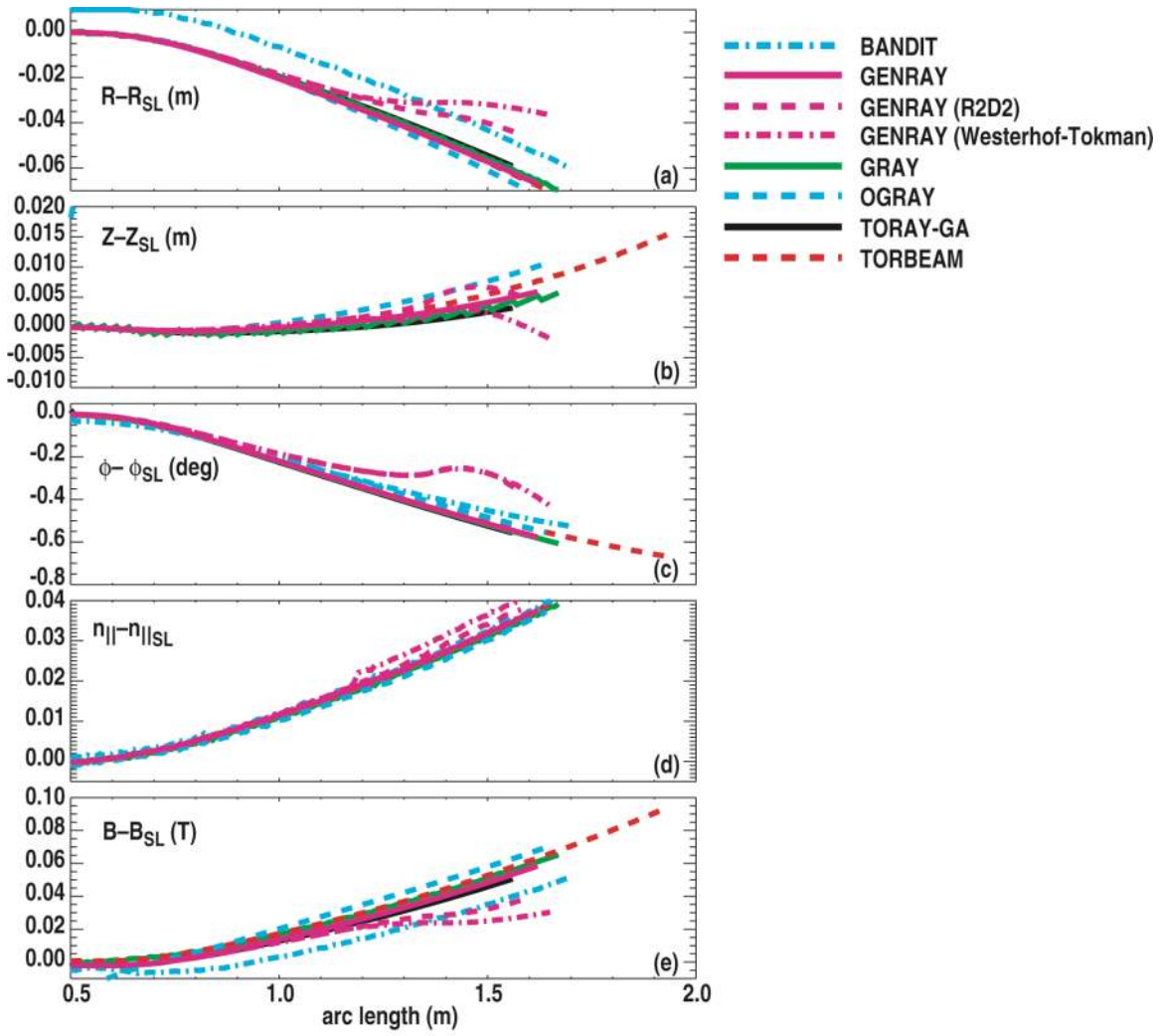NF_256426_PAP_5616, R. Prater, Figure 2

NF_256426_PAP_5616, R. Prater, Figure 3

Legend:
- BANDIT
- GENRAY
- GRAY
- OGRAY
- TORAY-FOM
- TORAY-GA
- TORBEAM

(a) $R - R_{SL}$ (m)

(b) $Z - Z_{SL}$ (m)

(c) $\phi - \phi_{SL}$ (deg)

(d) $n_{\parallel} - n_{\parallel SL}$
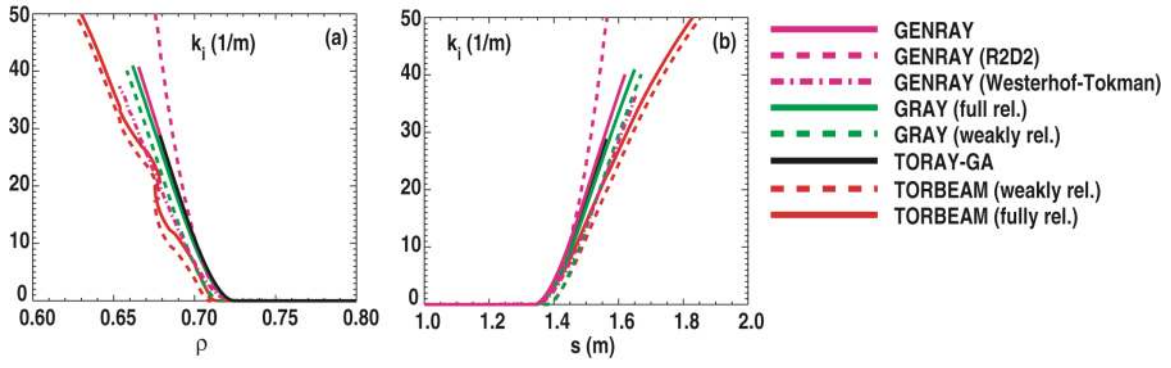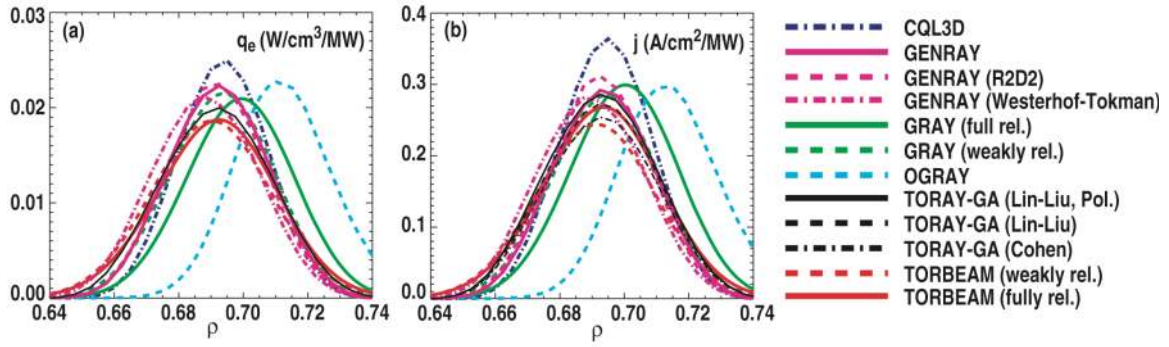
(e) $B - B_{SL}$ (T)
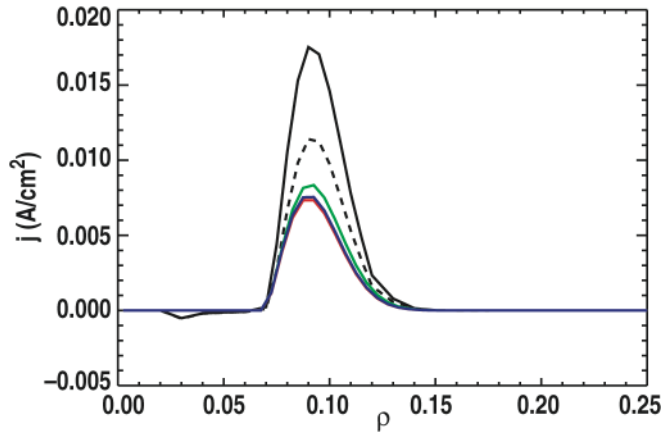
Arc Length (m)

NF_256426_PAP_5616, R. Prater, Figure 4

NF_256426_PAP_5616, R. Prater, Figure 5

NF_256426_PAP_5616, R. Prater, Figure 6

NF_256426_PAP_5616, R. Prater, Figure 7

NF_256426_PAP_5616, R. Prater, Figure 8

Legend:
- BANDIT
- GENRAY
- GENRAY (R2D2)
- GENRAY (Westerhof-Tokman)
- GRAY
- OGRAY
- TORAY-GA
- TORBEAM

NF_256426_PAP_5616, R. Prater, Figure 9

NF_256426_PAP_5616, R. Prater, Figure 10

Legend:
- CQL3D
- GENRAY
- GENRAY (R2D2)
- GENRAY (Westerhof-Tokman)
- GRAY (full rel.)
- GRAY (weakly rel.)
- OGRAY
- TORAY-GA (Lin-Liu, Pol.)
- TORAY-GA (Lin-Liu)
- TORAY-GA (Cohen)
- TORBEAM (weakly rel.)
- TORBEAM (fully rel.)

NF_256426_PAP_5616, R. Prater, Figure 11

NF_256426_PAP_5616, R. Prater, Figure 12